Baric, Valentin ; Ciacchi, Lucio Colombi ; Mädler, Lutz

Compaction-induced restructuring of aggregated nanoparticle films using the discrete element method

Journal Article as: peer-reviewed accepted version (Postprint)

DOI of this document*(secondary publication): https://doi.org/10.26092/elib/3166

Publication date of this document: 01/08/2024

* for better findability or for reliable citation

Recommended Citation (primary publication/Version of Record) incl. DOI:

Baric, Valentin ; Ciacchi, Lucio Colombi ; Mädler, Lutz. 2019. Compaction-induced restructuring of aggregated nanoparticle films using the discrete element method. In: Powder Technology, vol. 342. pp. 773-779. © Elsevier. DOI: 10.1016/j.powtec.2018.10.038.

Compaction-induced restructuring of aggregated nanoparticle films using the discrete element method

Valentin Baric [a,b], Lucio Colombi Ciacchi [a,c], Lutz Mädler [a,b,*]

[a] University of Bremen, Faculty of Production Engineering, Badgasteiner Str. 1, 28359 Bremen, Germany
[b] Leibniz Institute for Materials Engineering IWT, Badgasteiner Str. 3, 28359 Bremen, Germany
[c] University of Bremen, Hybrid Materials Interfaces Group, Am Fallturm 1, 28359 Bremen, Germany

A B S T R A C T

Aggregated nanoparticle films find application in many fields such as gas sensing, solar cells and batteries. These films are characterized by size distributions of polydisperse primary particles and sintered particle aggregates that dictate both the response to external load and functional properties such as heat or charge transport. Mechanical compaction of the films strongly affects these properties in a way that can be quantified by the change of porosity and pore size distributions on the applied compacting pressure. The exact restructuring mechanisms of the aggregate architecture, however, remain unknown. Here, we apply Discrete Element Method (DEM) simulations to gain access to such restructuring mechanisms in TiO_2 nanoparticle films synthesized by flame-spray pyrolysis. The ability of the sintered TiO_2 aggregates to rearrange via mutual detachment, rolling or sliding events dictated by non-covalent, humidity-dependent interactions are known to be crucial to predict the correct response to compaction. In this work, the importance of elastic deformation of aggregates according to a novel sinter bridge model is elucidated. The best match between DEM simulations and experiments is obtained for bridges with a tensile and bending strengths substantially larger than bulk TiO_2, consistently with a low probability of critical fracture initiation in nanometer-scale structures.

1. Introduction

Nanoparticle films composed of aggregates of primary particles deposited from the gas-phase in flame-based synthesis methods find attractive applications in catalysis [1,2], gas sensors [3–6], dye sensitized solar cells [7,8] and battery materials [9–11]. These films are often characterized by a high porosity up to 98%, a well-defined pore size distribution and a percolating particle network [12]. Especially the pore size distribution is important for applications involving fluid flows. These include the film imbibition with a second phase, e.g. a polymer matrix [13], and catalysis [5,14]. Here, the pores allow for the diffusion of fluids and therefore enable chemical reactions to take place at the particles' surface. In addition, charges can be conducted along the percolation paths [15].

Such a high porosity of the particle films, however, often comes with a low mechanical resistance. Thermal stabilization processes, i.e. annealing and sintering, can stabilize the films and enhance their electrical conductivity [16]. The drawbacks of thermal particle sintering are the resulting reduced porosity and specific surface area. Schopf et al. have developed an alternative two-roll lamination process [12] in which dry nanoparticle films were compacted at pressures up to 2.5 MPa. The compaction led to a significant increase in the films compressive Young's Modulus (from 0.8 MPa to 1.9 MPa) and a decrease in porosity from 84% to 79% while preserving the film's specific surface area. The electrical conductivity was enhanced due to an increased number of percolation paths [4]. In a follow-up study, Schopf et al. showed that compacted particle films maintain their structure against capillary forces resulting from an air-liquid interface during liquid imbibition [13]. This feature enables their utilization in many new applications.

The details of the restructuring during the compaction process, however, remain unclear. One challenge is to distinguish between the different contributions and roles of the film's hierarchical building blocks: primary particles, aggregates and agglomerates. In a series of recent studies, we have clearly identified the nature and extent of the non-covalent particle-particle contact forces between aggregates [17–20]. However, the mechanical strength of the covalent sinter bridges between primary particles within aggregates remains hardly accessible. Friedlander et al. reported elastic deformation and elongation of the bridges which led to significant restructuring of aggregate chains [21]. Seipenbusch et al. [22] argue that the sinter bridges between the primary particles are too strong to be broken during common film handling procedures. A quantitative evaluation using atomic force

* Corresponding author at: University of Bremen, Faculty of Production Engineering, Badgasteiner Str. 1, 28359 Bremen, Germany.
E-mail address: lmaedler@iwt.uni-bremen.de (L. Mädler).

microscopy (AFM) experiments on 1D-TiO_2 strings was carried out by Amin et al. [23]. They reported a decrease in the Young's Modulus and an increase in the tensile strength compared to bulk TiO_2, resulting from a low amount of lattice defects in such small dimensions.

We note that precise information about the particle connectivity and strength both within and among aggregates is crucial for the mechanical resistance and the electrical conductivity of the films. Regarding the latter, capillary bridges or van der Waals contacts between particles are characterized by a significantly lower electrical conductivity compared to sinter bridges [15]. A high number of broken sinter bridges during mechanical compaction might lead to a very different percolation structure and thus to different pathways for the transfer of charges across the film. This, in turn, may detrimentally affect their activity in gas sensing elements or their conductance when embedded in isolating matrices.

Simulations based on the discrete element method (DEM), as originally proposed by Cundall and Strack [24], are capable of simultaneously predicting the dynamical or mechanical behavior of systems composed of millions of particles. DEM is well established in a wide range of applications and a variety of interparticle contact models are available. Non-covalent interactions between primary particles in the range of a few nanometers are predominantly determined by a superposition of capillary forces at larger distances and solvation forces at shorter distance [17,20]. Dissipation arises because of the mutual sliding and rolling of particles in contact and is heavily dependent on the amount of solvent molecules in the contact region. In air, this is dictated primarily by the relative humidity and the amount of water adsorbed on the oxide surfaces [18]. In contrast, inertia and gravity are less important for the interactions of nanoparticles. The number of studies governing the interactions of nanoparticles is rather limited [25–28]. Only recently we have applied a combination of AFM force spectroscopy and molecular dynamic simulations to develop a new contact model suitable for DEM simulations of TiO_2 nanoparticle films [18,20]. The proposed model can represent TiO_2 primary particles below 20 nm considering normal and friction forces, as well as adhesion resulting from capillary and solvation forces. In doing so, however, we have assumed ideally rigid sinter bridges within aggregates, neglecting their possible bending or breaking. DEM simulations using these contact models were able to reproduce with sufficient accuracy the experimentally measured force response of the films upon tensile stress locally applied by means of an approaching and retracting AFM tip [18]. However, an overestimation of the simulated maximum forces was observed and tentatively ascribed to the simplistic description of rigid and unbreakable sinter bridges. Also, the transferability of the model to other loading situations has not been tested yet.

In this work, we extend and improve our previously developed DEM contact model with an additional covalent particle-particle bonding term that reproduces the correct mechanical behavior of sinter bridges in aggregates under mechanical stress. Particle bond models allowing for the breakage of bonds have been implemented into DEM for a variety of applications. These include the modelling of rocks [29], of the cementation of particles [30], of particle bonded with PVP binders [31], of maltodextrin agglomerates [32] and of a SiO_2 aggregate comprised of several thousand nanometer-sized primary particles [28]. However, the simulation of the mechanical compaction of complex nanoparticle films formed from polydisperse aggregates composed of non-rigid, breakable agglomerates [33], has not been attempted so far.

2. Material and methods

2.1. Experimental

TiO_2 aggregated nanoparticles were synthesized using flame spray pyrolysis (FSP) as described in detail in [12,34]. After generation, the particle films were laminated with pressures of 0.4, 1.2, 1.7, 2.3, 2.7 and 3.4 MPa. Primary particle and aggregate size distributions were derived from TEM image analyses and CPS disc centrifuge measurements as described in [18,35]. Porosity and pore size distributions were derived from nitrogen adsorption isotherms as described in detail in [12,13].

2.2. Simulations

2.2.1. Creation of particle film models

The deposition of nanoparticle aggregates was simulated as described in detail in [18,33]. Films were constructed with 600,000 primary particles in a tetragonal simulation box with lateral dimension of 2.0 μm × 2.0 μm in the x-y plane and initial height of 6.1 μm along the z axis. As also shown in [18], the primary particle sizes followed a log-normal distribution, as derived from TEM image analyses (median diameter of 9.0 nm and a geometrical standard deviation of 1.45). Aggregates including between 13 and 128 primary particles were generated randomly with a cluster-cluster aggregation algorithm as proposed by Filippov et al. [36]. The aggregates had a fractal dimension $D_f = 1.8$ with prefactor $k_f = 1.3$ and a mass mobility exponent $D_{fm} = 2.15$ with prefactor $k_m = 1.11$. Such parameters are commonly used to represent particles synthesized in the gas phase [37].

In-silico particle film formation determined by thermophoresis is computationally demanding, especially for low Peclet-numbers due to the high diffusivity of the aggregates. The ballistic deposition of aggregates reduces the computational time from weeks to seconds per CPU core. Mädler et al. [33] have found that the initial particle film structure depends on the Peclet number, which describes the ratio between convective and diffusive transport. This dependency, however, strongly decreases with increasing number of particles. Here we consider a broad aggregate size distribution (13–128 primary particles) in combination with a polydisperse primary particle size distribution, which resulted in the distribution of Peclet numbers shown in Fig. S1. Under these conditions, it is possible to neglect the effect of diffusion and the aggregates were deposited ballistically, which allowed us to generate sufficiently large particle films with reasonable computational effort.

2.2.2. Elastic sinter bridge model

Elastic sinter bridges within aggregates were modelled according to Potyondy and Cundall [29]. Bridges were defined at the beginning of each simulation only between pairs of particles of the same aggregate within a threshold distance $1.1^*(R_i + R_j)$, with R_i being the nominal radius of the particle i. Normal and tangential forces (F_n and F_t) and torques (M_n and M_t) on the bridges were calculated with the following set of equations [29]:

$$F_n = L^n \frac{E_B}{L_0} A_B \tag{1}$$

$$F_t = L^t \frac{E_B}{2L_0(1+\nu_B)} A_B \tag{2}$$

$$M_n = \delta^n \frac{E_B}{2L_0(1+\nu_B)} J \tag{3}$$

$$M_t = \delta^t \frac{E_B}{L_0} I \tag{4}$$

In Eqs. 1 and 2 the forces acting on a bridge with cross-section $A_B = \pi \cdot R_B^2$ and rest length L_0 depend linearly on the normal and tangential displacements L^n and L^t via the bridge Young's Modulus E_B and Poisson's ratio ν_B. In Eqs. 3 and 4 the torques are calculated from the relative tangential angular displacements δ^n and δ^t via the moment of inertia I and the polar moment of inertia J.

Brittle fracture occurred and the bridge was removed from the simulation if either the tensile or shear stress of the bridge exceeded the

threshold values σ_B and τ_B, according to:

$$-\frac{F_n}{A_B}+\frac{|M_t|}{I}R_B \geq \sigma_B \quad (5)$$

$$\frac{|F_t|}{A_B}+\frac{|M_n|}{J}R_B \geq \tau_B \quad (6)$$

Mixed stress and breakage models were neglected in accordance with [29].

The bridge rest length L_0 corresponded to the distance between the centers of mass of each pair of bonded particles, and the bridge radius was calculated as $R_B = \lambda \cdot R_{min}$, with R_{min} being the minimum between R_1 and R_2. (Table 1). The factor λ was determined from the measured particle and bridge radii of 118 bound primary particles in TEM images of flame-made TiO_2 nanoparticle aggregates, leading to an average value $\lambda = 0.48$. Literature values for E_B (56 GPa), σ_B and τ_B (4.2 GPa in both cases) [23] were used as a starting point for the DEM simulations, and were then varied to reproduce quantitatively the experimentally observed behavior of films under compaction (vide infra, Fig. S2).

The sinter bridge model is superimposed to the normal contact and adhesion model (vide infra). The effect of additional adhesion caused by the capillary forces is negligible as visible from Fig. S3.

All employed DEM parameters are summarized in Table 1.

2.2.3. DEM simulations

Discrete Element Method (DEM) simulations were performed with the open-source software LIGGGHTS, Version 3.5 [38]. The normal contact model considers non-linear Hertzian stress in combination with a viscous damping, which results from the viscosity of the water adsorbed at the particle surfaces within the contact area [18]. The energy dissipation by friction is modelled as constant torque (rolling friction) and a stick-slip behavior (sliding friction). Adhesion between non-aggregated primary particles is modelled as a superposition of capillary forces and solvation forces, based on a relative humidity of 50%, as described in detail in [18]. Gravity was neglected in all simulations. As in [18], a timestep of $\Delta t_t = 5{\cdot}10^{-13}$ s was used, equal to half the maximum timestep estimated from the Rayleigh time [39] $\Delta t_{crit} = 1{\cdot}10^{-12}$ s.

In the compaction simulations, two movable horizontal walls with the width of the simulation box were placed above and below the particle film to represent the lamination rolls of the experiment [12]. Particle-wall interactions were calculated using a Hertz-Mindlin model with a Young's Modulus of 56 GPa. Periodic boundary conditions were applied to the other film boundaries. The film porosity φ between the walls was calculated from the particle volume V_p and the total volume within the confined space between the walls V_{tot}: $\varphi = 1-\frac{V_p}{V_{tot}}$. The as-created particle films were first equilibrated until the total kinetic energy in the system reached a constant value (steady state) after about 5 μs of simulation time. This was necessary because the initial particle configuration was formed without consideration of the long-range interaction forces (adhesion forces) which are introduced during DEM. Hence, a film might be initialized in an unstable configuration. During this equilibration phase, a fictitious viscous force term of 100 pN/(m/s) was used to dissipate the kinetic energy and drive the aggregates stably towards a local energy minimum. This viscous force, however, had an insignificant effect on the following compaction of the film as reported in Fig. S4. After the equilibration, the upper wall was moved towards the lower wall with a constant velocity of 0.5 m/s, until a defined targeted pressure was reached. Then, the wall movement was reversed and the wall raised by 250 nm, which enabled a full expansion of the film without any further interaction between the walls and the particles. During this expansion, the normal pressure due to repulsive particle-particle interactions and bent sinter bridges was fully released, as indicated by a constant film porosity for at least 200 ns simulation time, after which the system was considered equilibrated. Test simulations were performed to ensure that the obtained variation of porosity with respect to the compaction pressure was neither dependent on the particular structure of the film (Fig. S5), nor influenced by boundary effects due to limited film size (Fig. S6).

The porosity of expanded particle films was calculated using a Monte Carlo approach as described in [40]. Random coordinates were selected within the film and it was evaluated whether a particle or a pore was selected. The ratio of the coordinates within pores to the total selected coordinates equals the porosity. This analysis considered 1 million coordinates per 10 nm film height. Simulated particle films are characterized by smaller dimensions than experimental films. Hence, the ratio of the surface to the bulk region was larger than in the experiments, which can result in overestimation of the calculated porosity. Therefore, a bulk region was defined by calculating the particle density profile along z integrated in x-y planes (Fig. S7). This density is constant in the bulk region and decreases towards the surface. Only this bulk region was considered for the analysis. This particle volume was also used to calculate an equivalent film volume V_{eq} for the experiments.

The pore size distributions (PSD) were calculated within the aforementioned bulk region using Monte Carlo simulations as presented by Bhattacharya and Gubbins [41]. Random coordinates within the pores of this region were selected and the largest spherical pore including this coordinate was calculated. From these information, a pore size distribution was derived. The authors showed, that these PSD are comparable to PSD obtained from nitrogen adsorption isotherms. Every few steps this PSD was compared to the previously determined PSD and a deviation was calculated. This routine continued until the deviation was lower than 0.1%. The shown cumulative distribution function Q_2 (d_{pore}) gives the fraction of the total pore area covered by pores with a diameter smaller than d_{pore}.

The breakage of sinter bridges was differentiated into normal and tangential breakage according to Eqs. 5 and 6, respectively. At every time step in the simulation, the aggregates containing a broken sinter bridge were evaluated. If the bridge fracture resulted in two separate

Table 1
Material and simulation parameters for the DEM. Different models were used for aggregate-aggregate interactions and sinter bridges within aggregates, respectively.

Particle-Particle interaction models	See [18]	Repulsive forces Capillary bridges Agglomerates
Young's modulus sinter bridge, E_B	56 GPa [23] (other values in Fig. S2,S8)	Sinter bridges
Tensile strength sinter bridge, σ_B	4.2 GPa [23], 15.0 GPa (other values in Fig. S2,S8)	Aggregates
Shear strength sinter bridge, τ_B	1.4 GPa, 4.2 GPa [23], 15.0 GPa (other values in Fig. S2,S8)	
Sinter bridge radius factor, λ	0.48	
Poisson's ratio sinter bridge, ν_B	0.28 [23]	
Viscosity (only during equilibration)	100 pN/(m/s)	
Time step Δt_t	$5{\cdot}10^{-13}$ s	

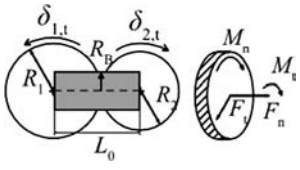

fragments (unconnected by other intact sinter bridges), each fragment was hereafter defined as an individual aggregate.

3. Results and discussion

3.1. Simulations of particle film compaction

After creation and equilibration of a particle film model, compaction simulations are performed as described in the Methods section and represented in Fig. 1. Namely, due to the action of the movable upper wall the film height and porosity decrease and the pressure acting on the walls increases. Inversion of the wall's movement leads to pressure release with an associated film expansion and slight increase of porosity up to a final equilibrium value that depend on the value of pressure at which the compaction is stopped.

The evolution of the pressure p as a function of the film height h is reported in Fig. 2a for simulations with elastic bridges with $E_B = 56$ GPa and two values of the tensile and shear strengths. They are compared to simulations performed with infinitely rigid, non-breakable aggregates and with only single primary particles not sintered together in aggregates (results for other choices of with E_B, σ_B and τ_B are reported in Fig. S2). In all simulations, three different stages are visible during the compaction: (1) an initial quick increase of the pressure; (2) a plateau region in which the film undergoes severe rearrangements while its height is massively reduced, leading to strong pressure fluctuation around a roughly constant value; (3) a further steep increase of the pressure at larger compaction, with much decreased mobility of the aggregates in the film.

The film behavior depends strongly on the properties of the sinter bridges, as it is also visible from the evolution of the transient film porosity during continuous compaction reported in Fig. 2b. Rigid aggregates result in the highest porosity and single particles in the lowest porosity at a given compaction pressure. Simulations using our elastic sinter bridge model result in intermediate porosities, although significantly closer to the single particle simulations. Decreasing the tensile and shear strength values from 15.0 GPa to 4.2 GPa leads to marginally smaller transient porosities.

3.2. Equilibrium porosities after compaction

The final equilibrium porosities φ and the equivalent film volumes V_{eq} obtained after compaction to a certain pressure and release of the

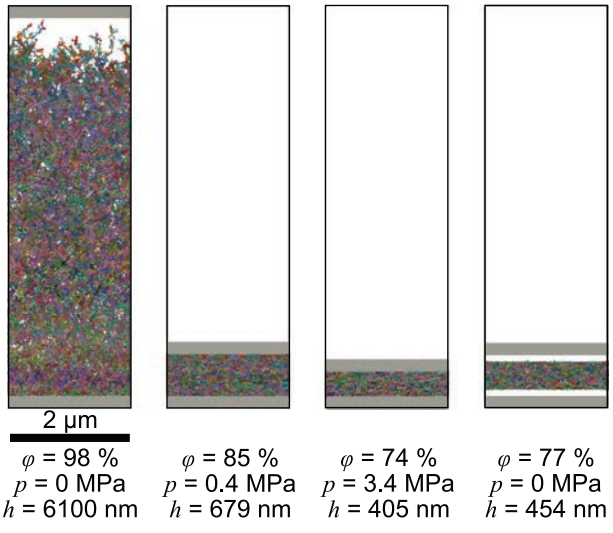

Fig. 1. Snapshots of a compaction simulation with $E_B = 56$ GPa and σ_B and τ_B equal to 15.0 GPa. The corresponding values of porosity φ, pressure p and film height h are reported under each snapshot. Particles belonging to the same aggregate are depicted with the same color. The hard walls compacting the film are represented with grey bars.

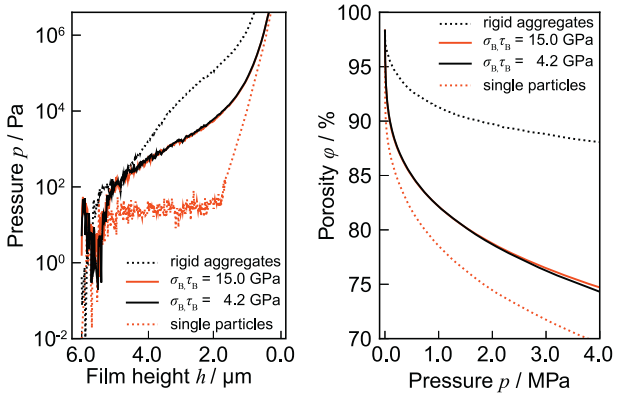

Fig. 2. a) Pressure-Distance curves for the compaction of the nanoparticle film. The pressure increase is shown for simulations using rigid aggregates, the elastic sinter bridge model and single particles. b) Porosities at given compaction pressure.

compression strain are shown in Fig. 3a and b, respectively, in comparison with experimental values. These two properties are connected via the relationship $V_{eq}(\varphi) = \frac{V_p}{1-\varphi}$. The equivalent volume $V_{eq}(\varphi)$ is most sensitive for large porosities, which makes it less suitable to detect minor structural changes at elevated pressures.

The experimentally obtained porosities decrease from 83% after compaction at 0.4 MPa to 76% at 3.4 MPa.

DEM simulations performed with infinitely rigid and non-breakable aggregates largely overestimate the film porosity at all pressure values, whereas simulations with single primary particles underestimate the porosity except for the smallest pressure value. Instead, excellent agreement with the experiments is obtained for simulations including the new bendable and breakable sinter bridge model. Especially setting the tensile and shear strengths to high values (σ_B,$\tau_B = 15.0$ GPa) leads to a perfect match of the φ and V_{eq} data for all compaction pressures, except for the smallest value. However, this single discrepancy can be explained by the fact that even before the lamination process the experimental films were subjected to some degree of compaction by

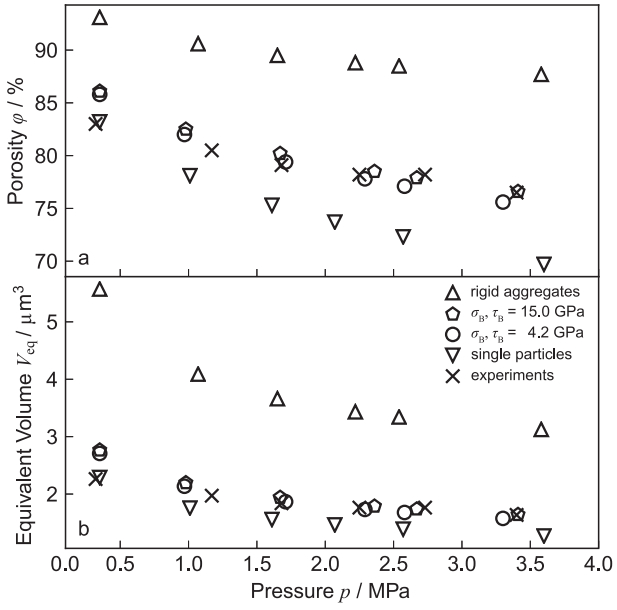

Fig. 3. Variation of the equilibrium porosity φ (a) and the equivalent volume V_{eq} (b) with respect to the compaction pressure after compaction experiments and DEM simulations (Fig. 1).

the action of the gas flow necessary to deposit the film from the gas phase onto the solid substrate.

3.3. Pore size distribution

The porosity of a film results from a variety of different structural features, including particle size, aggregate size, and pore structure. The pore size distribution (PSD) is sensitive to the exact structure of the pores and its correct prediction is therefore essential for a thorough validation of the here proposed DEM model with sinter bridges. Fig. 4a shows the cumulative distribution function $Q_2(d_{pore})$ of the PSD derived from both simulations ($\sigma_B,\tau_B = 15.0$ GPa) and experiments at several compaction pressures. All PSD are log-normal, with about 95% of the pore sizes ranging between 10 nm and 100 nm.

The median pore diameter in the experimentally obtained PSD is about 50 nm at 0.4 MPa and decreases to about 30 nm at 3.4 MPa. Simulations using the elastic sinter bridge model with $\sigma_B,\tau_B = 15.0$ GPa predict PSD in striking agreement with the experiments for all compaction pressures. The box plots in Fig. 4b show that the median pore diameters of the simulated films were only slightly lower (<3 nm) for all compaction pressures. Also, the inner 50% of all pores (displayed by the boxes) in the simulations agree with the respective experiments with only very low deviations. The $d_{97.5}$ value (97.5% of all pores are smaller than this value) of all simulations, however, are significantly smaller than in the experiments. This means that in the experiments a significant fraction of the pore area (Q_2) is covered by large pores ($d_{Pore} > 100$ nm), although only a few of them are sufficient to provide the necessary pore area. Since the simulated volume is much smaller than the experimental film dimensions, the probability for such large pores to appear is very low, which explains the apparent discrepancy.

Together with the results presented in Fig. 3, it can be concluded that at the lowest pressures the experimental films are characterized by less, but slightly larger pores than in the simulations. With increasing compaction pressure, the agreement improves both regarding the the number and the size of pores. Notably, simulations using either wholly rigid aggregates or single particles resulted in strong deviations from the experimental PSD. In both cases the resulting pores are larger, but the PSD are narrower in the former and broader in the latter case (blue and violet curves computed at 3.6 MPa in Fig. 4).

3.4. Sinter bridge breakage and aggregate size distribution

The applied sinter bridge model allows us to examine how many sinter bridges break (dependent on the material properties) and at which locations, an information that is not commonly accessible in experimental investigation. The fraction of the broken bridges with respect to the applied compaction pressure is shown in Fig. 5. Sinter bridges with $\sigma_B,\tau_B = 15.0$ GPa remained unbroken for all compaction pressures. A decrease in tensile and shear strength to $\sigma_B,\tau_B = 4.2$ GPa [23] caused a small fraction of sinter bridges (1.5% at 3.4 MPa compaction pressure) to break, as reported in Fig. 5.

The number of broken sinter bridges increases linearly with increasing compaction pressure. Therefore, the sinter bridge breakage was independent of the (constantly decreasing) aggregate size in this pressure range. The slope can be expected to slowly decrease after a much larger fraction of bridges break and the aggregate size becomes smaller. This is in fact observed in simulations using smaller tensile/shear strengths (see Fig. S8).

From the analysis of the DEM simulations in Fig. 5 we can also infer that almost the entirety of the sinter bridges break due to normal stress (Eq. 5) rather than tangential stress (Eq. 6). Since the tensile and shear strengths were assumed to be equal, the connectivity of the aggregates in the films seems to dictate much larger tensile than shear components on the sinter bridges. This might result from the fact that shear stress can be readily dissipated by the mutual sliding of the aggregates [18].

The spatial distribution of the broken sinter bridges within a compressed film ($\sigma_B,\tau_B = 4.2$ GPa) is shown in Fig. 6. The breakage locations are homogeneously distributed throughout the film, indicating a uniform distribution of stress.

Changes of the aggregate size distribution due to sinter bridge breakage and aggregate fragmentation are shown in Fig. 7. The median aggregate size decreases from 35 primary particles to 31 primary particles at 1.10 MPa and 27 primary particles at 3.40 MPa, in line with the linear increase of broken bridges (Fig. 5). The fragmentation proceeds with a rapid increase of the number of single particles in the films (0% initially, 6% at 1.10 MPa and 10% at 3.40 MPa). This suggests that the detachment of single primary particles from the edges of stressed aggregates (as shown in Fig. 7b) is a frequent mode of fragmentation during film compaction.

4. Conclusion

In this work, DEM simulations were successfully applied to investigate the compaction of films composed of polydisperse nanoparticle aggregates. A ballistically deposited particle film with the dimensions of 2.0 μm × 2.0 μm × 6.1 μm containing 600,000 polydisperse primary particles (approx. 10 nm in diameter) was suitable to represent structural properties of experimental films such as porosity and pore size distribution.

The changes of these properties after compaction at different pressures, which was experimentally realized in a previously described lamination process [12], could be predicted with great accuracy in DEM simulations only if the presence of elastic sinter bridges between primary particles in aggregates was taken into account. In particular, simulations of films composed of either single particles interacting only via

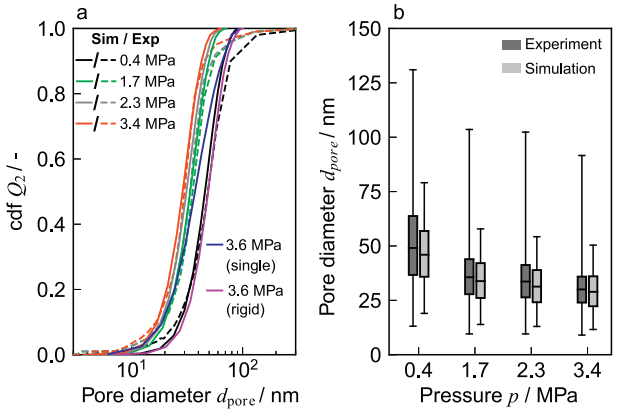

Fig. 4. a) Pore size distributions for experimental and simulated particle films ($\sigma_B,\tau_B = 15.0$ GPa). b) Box plots of the pore size distributions. The box represents the region of probability between 25% and 75%. The whiskers denote 2.5% and 97.5% (inner 95%) of the values and the horizontal lines show the median pore diameters.

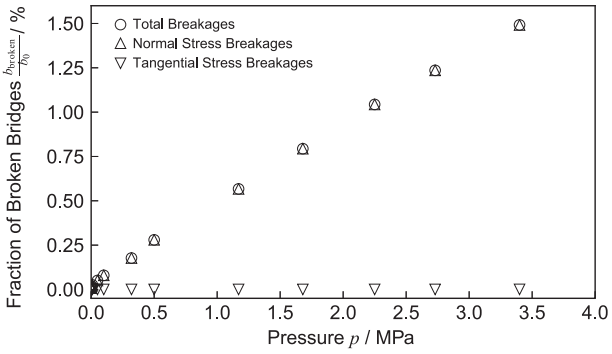

Fig. 5. The fraction of broken sinter bridges in total and caused by normal and tangential stress for simulations with $\sigma_B,\tau_B = 4.2$ GPa.

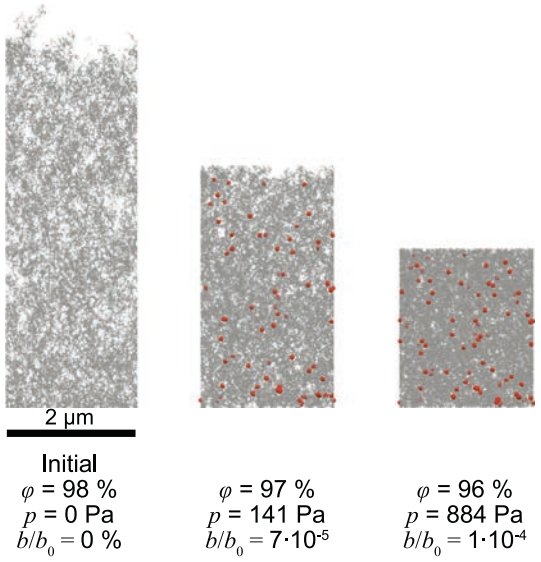

Fig. 6. Snapshots of a DEM compaction simulation (σ_B,τ_B = 4.2 GPa) along with their respective porosity φ, compaction pressure p and ratio of broken sinter bridges b/b_0 (the compacting walls are not shown). The red spots highlight locations of broken sinter bridges. (For interpretation of the references to color in this figure legend, the reader is referred to the web version of this article.)

non-covalent adhesion terms or infinitely rigid and non-breakable aggregates resulted in dependencies of the porosity and pore size distribution upon the applied pressure significantly different than in the experiments (Figs. 3 and 4).

We found that the best match to experimentally measured porosities and pore size distributions after lamination was achieved considering elastic sinter bridges with a Young's Modulus of 56 GPa and with tensile and shear strengths of 15.0 GPa. These strength values are larger than those used to characterize extended TiO_2 systems (4.2 GPa [23]), which resulted in a slight underestimation of the porosity with respect to the compaction pressure (Fig. 3) and about 1.5% of broken sinter bridges. In fact, it can be expected that sinter bridges of dimensions of the order of 10 nm are characterized by a low probability of containing critical defects from which brittle fracture can originate. It is thus reasonable to assume that stable sinter bridges at this size scale prevent fragmentation of the aggregates even during harsh film handling such as compaction at pressures of several MPa.

Crucial, though, is the ability of the aggregates to elastically deform according to the here-proposed sinter bridge model. This is additional to mutual detachment, rolling or sliding events dictated by the non-covalent, humidity-dependent interactions investigated in our earlier works [17–20]. The implementation of the sinter bridge model

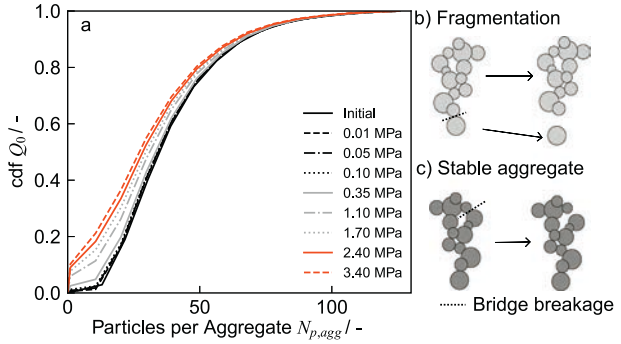

Fig. 7. The cumulative distribution function Q_0 of the aggregate size distribution for several compaction pressures (simulations with σ_B,τ_B = 4.2 GPa). An increase of the compaction pressures results in a larger number of small aggregates due to fragmentation (b). Note that not every bridge breakage leads to fragmentation (c).

completes the constitutive model to represent aggregated TiO_2 nanoparticles smaller than 20 nm in diameter. Until today, the model is only validated for this material and size range. We assume, however, that the model can be valid for all hydrophilic materials in this size range, because the interactions are mainly determined by the adsorbed water layer. This includes a large variety of particles. The extension of the model towards larger particles, can easily be achieved because the capillary force model converges towards classical theory, valid for particle diameters larger than 20 nm. Interactions at this large particle size can also be calculated without solvation forces, which simplifies the model further. It has to be noted, however, that a significant increase in diameter of the sinter bridges also increases the probability for lattice defects and, therefore, decreases the tensile/shear strength. We highly recommend additional validation in this case.

We consider this new model as a key step to understand how structural and functional film properties including percolation, pore structure, heat transfer and electric conductivity are affected by various mechanical load scenarios associated with post-synthesis handling steps. Using this understanding, it may be possible to tailor the film properties to match the needs of a broad class of applications, e.g. in catalysis [1,2], gas sensing [4,6], and energy storage [9–11] or production [3,34].

Acknowledgements

The authors thank Sven Schopf and Tobias Wollborn for the conduction of the experimental analysis. This work has been funded by the DFG under grants MA 3333/3, CO 1043/3 and under grants MA3333/10-1 and HA2420/16-1. Computational time has been provided by the North-German Supercomputing Alliance (HLRN) at Hannover and Berlin, Germany.

Appendix A. Supplementary data

Supplementary data to this article can be found online at https://doi.org/10.1016/j.powtec.2018.10.038.

References

[1] H.K. Grossmann, T. Grieb, S. Schopf, Y.H. Ng, R. Amal, L. Mädler, Flame-made oxide heterojunctions for photocatalytic water splitting, Chemie Ingenieur Technik 86 (2014) (1433–1433).
[2] M. Minnermann, H.K. Grossmann, S. Pokhrel, K. Thiel, H. Hagelin-Weaver, M. Bäumer, L. Mädler, Double flame spray pyrolysis as a novel technique to synthesize alumina-supported cobalt Fischer–Tropsch catalysts, Catal. Today 214 (2013) 90–99.
[3] L. Mädler, A. Roessler, S.E. Pratsinis, T. Sahm, A. Gurlo, N. Barsan, U. Weimar, Direct formation of highly porous gas-sensing films by in situ thermophoretic deposition of flame-made Pt/SnO_2 nanoparticles, Sensors Actuators B Chem. 114 (2006) 283–295.
[4] J. Kemmler, S.O. Schopf, L. Mädler, N. Barsan, U. Weimar, New process technologies for the deposition of semiconducting metal oxide nanoparticles for sensing, Procedia Eng. 87 (2014) 24–27.
[5] J.A.H. Dreyer, N. Riefler, G.R. Pesch, M. Karamehmedovic, U. Fritsching, W.Y. Teoh, L. Mädler, Simulation of gas diffusion in highly porous nanostructures by direct simulation Monte Carlo, Chem. Eng. Sci. 105 (2014) 69–76.
[6] J.A. Kemmler, S. Pokhrel, L. Mädler, U. Weimar, N. Barsan, Flame spray pyrolysis for sensing at the nanoscale, Nanotechnology 24 (2013), 442001.
[7] M. Zukalova, A. Zukal, L. Kavan, M.K. Nazeeruddin, P. Liska, M. Grätzel, Organized mesoporous TiO_2 films exhibiting greatly enhanced performance in dye-sensitized solar cells, Nano Lett. 5 (2005) 1789–1792.
[8] J. van de Lagemaat, K.D. Benkstein, A.J. Frank, Relation between particle coordination number and porosity in nanoparticle films: implications to dye-sensitized solar cells, J. Phys. Chem. B 105 (2001) 12433–12436.
[9] M. Gockeln, S. Pokhrel, F. Meierhofer, J. Glenneberg, M. Schowalter, A. Rosenauer, U. Fritsching, M. Busse, L. Mädler, R. Kun, Fabrication and performance of $Li_4Ti_5O_{12}$/C Li-ion battery electrodes using combined double flame spray pyrolysis and pressure-based lamination technique, J. Power Sources 374 (2018) 97–106.
[10] M. Gockeln, J. Glenneberg, M. Busse, S. Pokhrel, L. Mädler, R. Kun, Flame aerosol deposited $Li_4Ti_5O_{12}$ layers for flexible, thin film all-solid-state Li-ion batteries, Nano Energy 49 (2018) 564–573.
[11] F. Meierhofer, H. Li, M. Gockeln, R. Kun, T. Grieb, A. Rosenauer, U. Fritsching, J. Kiefer, J. Birkenstock, L. Mädler, S. Pokhrel, Screening precursor–solvent combinations for

$Li_4Ti_5O_{12}$ energy storage material using flame spray pyrolysis, ACS Appl. Mater. Interfaces 9 (2017) 37760–37777.
[12] S.O. Schopf, S. Salameh, L. Mädler, Transfer of highly porous nanoparticle layers to various substrates through mechanical compression, Nanoscale 5 (2013) 3764–3772.
[13] S.O. Schopf, A. Hartwig, U. Fritsching, L. Mädler, Imbibition into highly porous layers of aggregated particles, Transp. Porous Media (2017) 1–23.
[14] G.R. Pesch, N. Riefler, U. Fritsching, L. Colombi Ciacchi, L. Mädler, Gas-solid catalytic reactions with an extended DSMC model, AICHE J. 61 (2015) 2092–2103.
[15] N. Riefler, L. Mädler, Structure-conductivity relations of simulated highly porous nanoparticle aggregate films, J. Nanopart. Res. 12 (2010) 853–863.
[16] A. Tricoli, M. Graf, F. Mayer, S. Kühne, A. Hierlemann, S.E. Pratsinis, Micropatterning layers by flame aerosol deposition-annealing, Adv. Mater. 20 (2008) 3005–3010.
[17] S. Salameh, J. Schneider, J. Laube, A. Alessandrini, P. Facci, J.W. Seo, L.C. Ciacchi, L. Mädler, Adhesion mechanisms of the contact interface of TiO_2 nanoparticles in films and aggregates, Langmuir 28 (2012) 11457–11464.
[18] J. Laube, V. Baric, S. Salameh, L. Mädler, L. Colombi Ciacchi, A new contact model for the discrete element method simulation of TiO_2 nanoparticles films under mechanical load, Granul. Matter 20 (2018) 1–16.
[19] J. Laube, M. Dörmann, H.J. Schmid, L. Mädler, L. Colombi Ciacchi, Dependencies of the adhesion forces between TiO_2 nanoparticles on size and ambient humidity, J. Phys. Chem. C 121 (2017) 15294–15303.
[20] J. Laube, S. Salameh, M. Kappl, L. Mädler, L. Colombi Ciacchi, Contact forces between TiO_2 nanoparticles governed by an interplay of adsorbed water layers and roughness, Langmuir 31 (2015) 11288–11295.
[21] S.K. Friedlander, K. Ogawa, M. Ullmann, Elasticity of nanoparticle chain aggregates: Implications for polymer fillers and surface coatings, Powder Technol. 118 (2001) 90–96.
[22] M. Seipenbusch, S. Rothenbacher, M. Kirchhoff, H.J. Schmid, G. Kasper, A.P. Weber, Interparticle forces in silica nanoparticle agglomerates, J. Nanopart. Res. 12 (2010) 2037–2044.
[23] S.S. Amin, S.Y. Li, X. Wu, W. Ding, T.T. Xu, Facile synthesis and tensile behavior of TiO_2 one-dimensional nanostructures, Nanoscale Res. Lett. 5 (2009) 338–343.
[24] P.A. Cundall, O.D.L. Strack, A discrete numerical model for granular assemblies, Geotechnique 29 (1979) 47–65.
[25] R. Moreno-Atanasio, S.J. Antony, R.A. Williams, Influence of interparticle interactions on the kinetics of self-assembly and mechanical strength of nanoparticulate aggregates, Particuology 7 (2009) 106–113.
[26] M.Q. Chandler, J.F. Peters, D. Pelessone, Discrete element modeling of calcium-silicate-hydrate, Model. Simul. Mater. Sci. Eng. 21 (2013), 055010.
[27] G.S. Boltachev, K.E. Lukyashin, V.A. Shitov, N.B. Volkov, Three-dimensional simulations of nanopowder compaction processes by granular dynamics method, Phys. Rev. E 88 (2013) (12209–12209).
[28] C. Schilde, C.F. Burmeister, A. Kwade, Measurement and simulation of micromechanical properties of nanostructured aggregates via nanoindentation and DEM-simulation, Powder Technol. 259 (2014) 1–13.
[29] D.O. Potyondy, P.A. Cundall, A bonded-particle model for rock, Int. J. Rock Mech. Min. Sci. 41 (2004) 1329–1364.
[30] L. Brendel, J. Török, R. Kirsch, U. Bröckel, A contact model for the yielding of caked granular materials, Granul. Matter 13 (2011) 777–786.
[31] M. Dosta, S. Dale, S. Antonyuk, C. Wassgren, S. Heinrich, J.D. Litster, Numerical and experimental analysis of influence of granule microstructure on its compression breakage, Powder Technol. 299 (2016) 87–97.
[32] A. Spettl, S. Bachstein, M. Dosta, M. Goslinska, S. Heinrich, V. Schmidt, Bonded-particle extraction and stochastic modeling of internal agglomerate structures, Adv. Powder Technol. 27 (2016) 1761–1774.
[33] L. Mädler, A.A. Lall, S.K. Friedlander, One-step aerosol synthesis of nanoparticle agglomerate films: simulation of film porosity and thickness, Nanotechnology 17 (2006) 4783–4795.
[34] L. Mädler, H.K. Kammler, R. Mueller, S.E. Pratsinis, Controlled synthesis of nanostructured particles by flame spray pyrolysis, J. Aerosol Sci. 33 (2002) 369–389.
[35] S. Salameh, R. Scholz, J.W. Seo, L. Mädler, Contact behavior of size fractionated TiO_2 nanoparticle agglomerates and aggregates, Powder Technol. 256 (2014) 345–351.
[36] A. Filippov, M. Zurita, D. Rosner, Fractal-like aggregates: relation between morphology and physical properties, J. Colloid Interface Sci. 229 (2000) 261–273.
[37] S.K. Friedlander, Smoke, Dust, and Haze: Fundamentals of Aerosol Dynamics, Oxford University Press, Oxford, 2000.
[38] C. Kloss, C. Goniva, A. Hager, S. Amberger, S. Pirker, Models, algorithms and validation for opensource DEM and CFD-DEM, Prog. Comput. Fluid Dyn. 12 (2012) 140–152.
[39] Y.J. Li, Y. Xu, C. Thornton, A comparison of discrete element simulations and experiments for 'sandpiles' composed of spherical particles, Powder Technol. 160 (2005) 219–228.
[40] L.D. Gelb, K.E. Gubbins, Characterization of porous glasses: simulation models, adsorption isotherms, and the Brunauer-Emmett-Teller analysis method, Langmuir 14 (1998) 2097–2111.
[41] S. Bhattacharya, K.E. Gubbins, Fast method for computing pore size distributions of model materials, Langmuir 22 (2006) 7726–7731.